Nanoscale force sensing of an ultrafast nonlinear optical response

Zeno Schumacher[a,1,2], Rasa Rejali[a], Raphael Pachlatko[a], Andreas Spielhofer[a], Philipp Nagler[b], Yoichi Miyahara[a], David G. Cooke[a], and Peter Grütter[a,1]

[a]Department of Physics, McGill University, Montreal QC H3A 2T8, Canada; and [b]Department of Physics, University of Regensburg, 93053 Regensburg, Germany

Edited by Jianming Cao, Florida State University, Tallahassee, FL, and accepted by Editorial Board Member Zachary Fisk July 2, 2020 (received for review March 2, 2020)

The nonlinear optical response of a material is a sensitive probe of electronic and structural dynamics under strong light fields. The induced microscopic polarizations are usually detected via their far-field light emission, thus limiting spatial resolution. Several powerful near-field techniques circumvent this limitation by employing local nanoscale scatterers; however, their signal strength scales unfavorably as the probe volume decreases. Here, we demonstrate that time-resolved atomic force microscopy is capable of temporally and spatially resolving the microscopic, electrostatic forces arising from a nonlinear optical polarization in an insulating dielectric driven by femtosecond optical fields. The measured forces can be qualitatively explained by a second-order nonlinear interaction in the sample. The force resulting from this nonlinear interaction has frequency components below the mechanical resonance frequency of the cantilever and is thus detectable by regular atomic force microscopy methods. The capability to measure a nonlinear polarization through its electrostatic force is a powerful means to revisit nonlinear optical effects at the nanoscale, without the need for emitted photons or electrons from the surface.

atomic force microscopy | time-resolved | nonlinear optics

Defects determine the properties of real-world materials. As an example, in optoelectronic materials, structural imperfections lead to charge traps, recombination sites, and other efficiency limitations when converting light to electricity (or vice versa). These defects ultimately determine the lifetime and thus economic viability of the material for a particular application. A major experimental challenge is the characterization of the structure–property relation of the diversity of defects in a given material as a function of processing conditions or composition. On a more fundamental level, the motion of single molecules, conformation changes during chemical reactions, electron dynamics in solids, and the effects of defects or trap states on electron motion and behavior are among many fundamental processes waiting to be observed at the femtosecond and nanometer scale (1). Achieving simultaneous spatial and temporal resolution on the relevant length (nanometer) and time scales (10 fs to 100 fs) is a holy grail in material science. Atomic force microscopy (AFM) can be used to obtain atomically resolved structural data on insulators, semiconductors, and metals in any environment, including in physiological solutions.

Here, we demonstrate measurements on the femtosecond time scale of the optically induced polarization in lithium niobate by force detection using time-resolved AFM (tr-AFM) at room temperature in ultrahigh vacuum (UHV). We take advantage of the second-order nonlinear susceptibility of lithium niobate to generate an electric polarization induced by two laser pulses with ∼100-fs width. The change in electric polarization in the sample is measured as a function of delay times through the change in force by using noncontact AFM (nc-AFM). In AFM, the spatial resolution is determined by the tip radius, in our system, typically on the order of a few nanometers.

Results

We split the output of a mode-locked femtosecond fiber laser operating at 80-MHz repetition rate and 780-nm central wavelength, 200 mW (Toptica FemtoFiber pro NIR), to generate two coherent pulse trains, with a well-defined temporal delay between the two. The pulse trains can be arranged in a noncollinear or collinear fashion and focused onto the tip–sample junction of an AFM incorporated in a UHV system. As the two pulses are delayed with respect to each other, the light intensity at the tip–sample junction oscillates, in delay time, with the period of the laser illumination (∼2.6 fs). A sketch of the system is shown in Fig. 1. In our setup, the tip is held in a fixed position, and the sample is scanned to measure the spatial variations of the sample response to the optical stimulation simultaneously with regular AFM images. The laser beam is aligned and focused relative to the tip, and thereby remains fixed during the experiment.

Lithium niobate is an insulator with a band gap of 3.78 eV (2), a noncentrosymmetric crystal structure, and a large second-order optical nonlinear susceptibility $\chi^{(2)}$. In general, the electric field

Significance

Optical properties of materials are governed by nanoscale charge motion induced by ultrafast light fields. Here, we demonstrate that the electrostatic force originating from light-induced electron motion in a dielectric can be measured using atomic force microscopy. We observe changes in the force originating from second-order nonlinear optical interactions in the sample on a sub-15-nm scale and 100-fs time resolution. The time resolution is set by the light pulse characteristics, not by the properties of the force sensor. Our method does not rely on nonlinear tip–sample interactions, thus advancing the possibility to observe ultrafast nonlinear light–matter interactions with spatial resolution in any material. We envision this technique will allow the correlation of nanometer structure with light-induced time-resolved kinetics.

Author contributions: Z.S., D.G.C., and P.G. designed research; Z.S., R.R., R.P., A.S., and Y.M. performed research; P.N. contributed new reagents/analytic tools; Z.S. and R.R. analyzed data; Z.S., R.R., R.P., A.S., and Y.M. maintained and improved the experimental setup; P.N. fabricated the $MoSe_2$ sample; P.G. supervised the experiment; and Z.S., R.R., D.G.C., and P.G. wrote the paper.

The authors declare no competing interest.

This article is a PNAS Direct Submission. J.C. is a guest editor invited by the Editorial Board.

[1]To whom correspondence may be addressed. Email: zenos@physics.mcgill.ca or peter.grutter@mcgill.ca.

[2]Present address: Department of Physics, ETH Zurich, 8093 Zurich, Switzerland.

This article contains supporting information online at https://www.pnas.org/lookup/suppl/doi:10.1073/pnas.2003945117/-/DCSupplemental.

First published August 4, 2020.

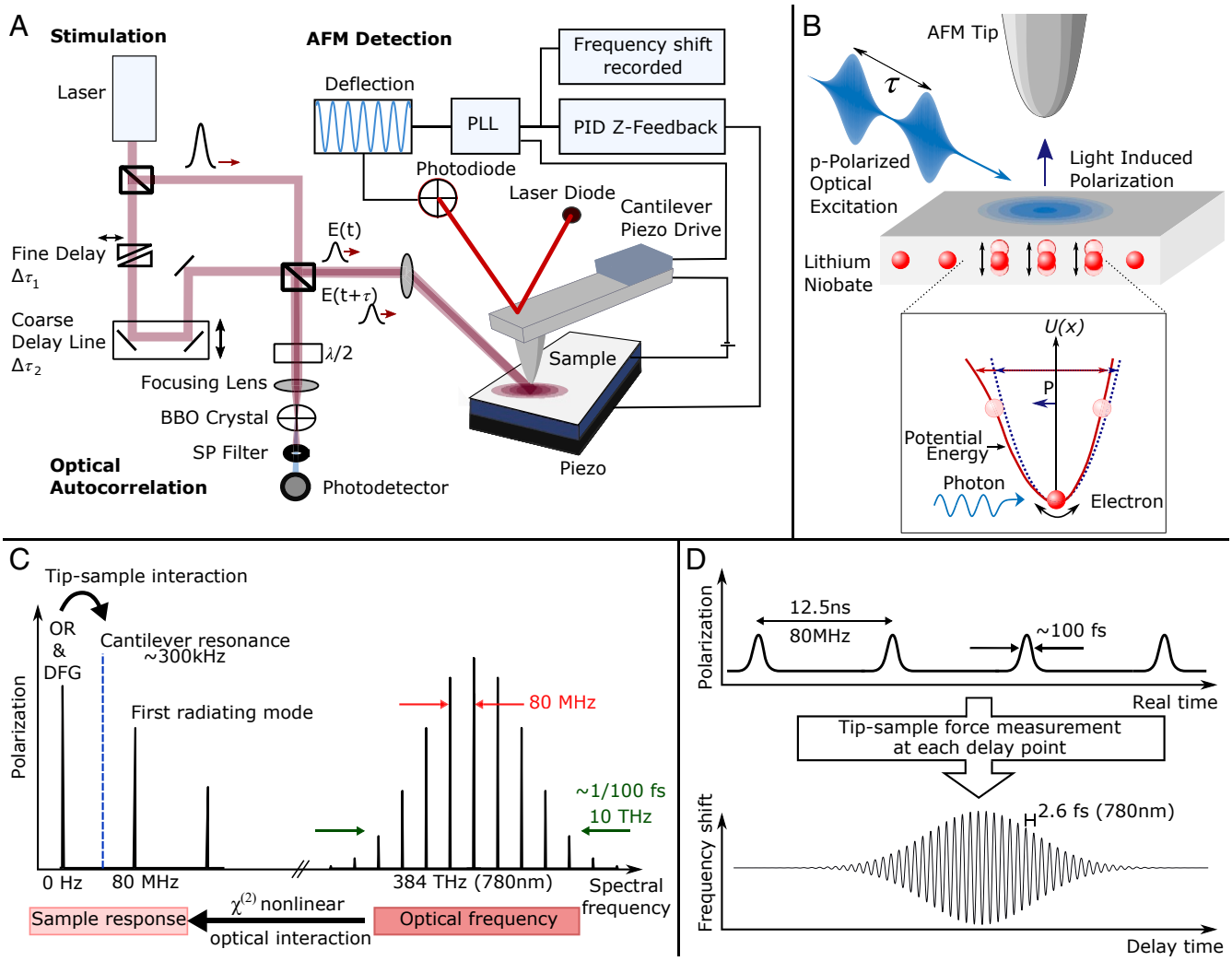

Fig. 1. (*A*) Illustration of the experimental setup and beam alignment. An ultrafast laser is incorporated into an UHV-AFM. The laser beam is split, and one beam is time delayed, before both beams are recombined and focused into the UHV chamber. The beam impinges on the sample surface with an angle of $\sim 80^\circ$ relative to the surface normal. (*B*) The ultrafast pulses, with τ denoting the relative temporal delay between the two, incident on the sample surface. The optical stimulation causes the electrons in the nonlinear medium to oscillate in the anharmonic potential of a noncentrosymmetric crystal (solid line), thereby generating a net static polarization. A purely parabolic potential (dashed line), characteristic of a linear medium, is shown for reference. (*C*) Spectral frequency sketch of the occurring signal. The $\chi^{(2)}$ nonlinear interaction is converting the optical frequency down to a quasi-DC sample response (0 Hz), which, in turn, is detected by the AFM through the tip–sample interaction. (*D*) Time domain representation of the nonlinear polarization repeating at the repetition rate of the laser with a duration of the pulse overlap. The AFM measurement in delay time samples the nonzero averaged component (quasi-DC, 0 Hz) of this nonlinear polarization at each delay step, resulting in the sketched interference measurement.

of an impinging laser pulse causes electrons in the medium to oscillate around the potential minimum. However, in a nonlinear material, such as lithium niobate, this potential is no longer purely parabolic, due to the higher-order perturbations, and the resultant motion of the electrons in the potential well leads to a net quasi-DC electric polarization, known as optical rectification, as shown in Fig. 1 (3). Optical rectification does not carry any information about the phase of the optical carrier wave, but instead gives rise to a polarization that follows the envelope of the laser pulse.

More generally, when two nonresonant intense electric fields are incident on a material with a nonzero second-order susceptibility, the resultant nonlinear polarization is described by (4)

$$P^{(2)}(t) = \epsilon_0 \chi^{(2)} [\tilde{E}(t) + \tilde{E}(t+\tau)]^2, \qquad [1]$$

where $\tilde{E}(t) = E(t)e^{-i\omega t} + E^\star(t)e^{i\omega t}$, with the pulse envelope $E(t)$ and ω denoting the carrier frequency. From Eq. **1**, the well-known nonlinear effects, such as optical rectification (*OR*), sum frequency generation (*SFG*), difference frequency generation (*DFG*), and second harmonic generation (*SHG*) follow (see *Materials and Methods* for details).

Second-order interactions between pulses with the same center frequency lead to quasi-DC polarizations. Here we separate these polarizations into two parts: those arising from interactions of a pulse with itself $P^{(2)}_{OR}(t)$ and between two separate and time delayed pulses $P^{(2)}_{OR}(t,\tau)$. The resulting polarization from this $P^{(2)}_{OR}(t,\tau)$ term

$$P^{(2)}_{OR}(t,\tau) = \epsilon_0 \chi^{(2)} E(t) E^\star(t+\tau) e^{-i\omega\tau} \qquad [2]$$

oscillates with respect to the delay time, τ, with a period of $2\pi/\omega$, and follows the envelope $E(t)$ in real time t. This quasi-DC polarization retains the information about the phase difference between the two pulses. Even though this term has no

oscillating field in real time t it is still pulsed at the laser repetition rate of 80 MHz (Fig. 1 *C* and *D*). AFM can probe the quasi-static electric field originating from $P^{(2)}_{OR}(t,\tau)$, and resolve any changes in the electric field arising from a change in delay between the two beams without phase matching errors due to the nanometer-sized probe volume. Additionally, the $P^{(2)}_{OR}(t)$ term, which is not oscillating with delay time, will be present, resulting in a constant background (see *Materials and Methods*). The electrostatic force probed by the AFM can be written as (5 and 6)

$$F_{elec} = \frac{1}{2}\frac{dC}{dz}\left(V_{cpd} - V_{dc} - \frac{\phi_{pol}}{e}\right)^2, \qquad [3]$$

with the tip–sample capacitance C, the contact potential difference between the tip and the sample V_{cpd}, and the tip–sample distance z. The potential arising due to the light-induced polarization in the material is denoted by ϕ_{pol}, which contains the one- and two-beam polarization terms $P^{(2)}_{OR}(t)$ and $P^{(2)}_{OR}(t,\tau)$.

tr-AFM Measurements on Lithium Niobate. Lithium niobate as a bulk crystal is extensively used in nonlinear optics and, with its large band gap, is a good benchmark for nonresonant optical nonlinearities.

In frequency modulation AFM (FM-AFM), a cantilever oscillating (6-nm amplitude) at its resonance frequency is brought into close proximity to the sample; tip–sample forces are thus measured by recording the resonance frequency shift of the cantilever (7). The z-cut crystal of lithium niobate, in conjunction with p-polarized incident light, allows for the strongest induced polarization occurring along the surface normal. Fig. 2*A* shows the recorded frequency shift while the two beams are delayed with respect to each other. An oscillating response (period 2.6 fs) during pulse overlap is measured as expected ($\lambda/c = 2.6$ fs) due to the nonresonant and instantaneous response of the electrons. This indicates that only the optical pulse duration, specifically, the number of optical field cycles in the excitation pulses, limits the temporal resolution of this technique. The measured signal can qualitatively be modeled by Eq. **9** (see *Materials and Methods* for details). *SI Appendix*, Figs. S2 and S4 shows a comparison of the calculated and measured signal.

Using an AFM tip as our force detector not only grants us high spatial resolution; in addition, the small probing volume of the AFM tip ensures that phase matching is always satisfied (Fig. 2). As expected, the interferometric optical autocorrelation exhibits fast oscillations (Fig. 2*B*), while the noncollinear autocorrelation (Fig. 2*D*) simply traces the intensity overlap of the two pulses. The concurrently recorded AFM measurement, on the other hand, shows a fast oscillating signal in collinear as well as a noncollinear arrangement. While a traditional macroscopic measurement of a noncollinear autocorrelation has no phase sensitivity due to the spatial averaging between the two pulses, the AFM measurement detects the interference of the pulses from a much smaller volume compared to the scale of the optical interference fringes.

The incorporation of the ultrafast laser source does not necessitate modifications on the AFM, and thereby the microscopy retains its intrinsic nanometer spatial resolution. Thus, the tr-AFM signal can be spatially mapped by repeating the pump–probe delay scan at each point on the sample surface. Fig. 3*A* shows a topography image recorded in FM-AFM mode of an HF-etched periodically poled lithium niobate (PPLN) sample (for large-scale image, see *SI Appendix*, Fig. S5). The etching creates a ∼120-nm height difference between the regions with different poling directions (8). The height changes gradually over a lateral extent of 200 nm to 400 nm, depending on the location (see height profile in *SI Appendix*, Fig. S5). The dotted line indicates the location of each delay scan. The amplitude of the tr-AFM signal shows a strong attenuation, which is likely due to a surface adsorbent situated at the boundary between two oppositely polarized regions (Fig. 3*C*), and is recovered when the upper terrace of the PPLN is reached. The tr-AFM signal is normalized by the optically measured autocorrelation intensity to account for any small fluctuation in laser power during the measurement time. To illustrate the significant drop of the ultrafast signal within a few tens of nanometers, the full delay scans taken at the two positions are plotted in Fig. 3*D*. Within two consecutive steps of 12.25 nm each (see line scan in Fig. 3*C*), the tr-AFM signal drops by 30%, followed by another drop of 40%. This clearly demonstrates that the tr-AFM signal can be used to probe spatial variations of the sample response on a sub-15-nm scale in our setup.

We note that the fast oscillations observed in the AFM scan can be used to determine the minimal achievable delay step that results in a resolvable frequency shift change. Fig. 3*E* is a measurement of the cantilever frequency shift at a constant height while the delay between the two pulse trains is swept. Two data points are taken at each delay step, with each averaged for 2 ms. We can distinguish two data points separated by the minimum delay step achievable with our double-wedge time delay setup. The minimal measurable delay time is 25 as due to the delay setup and not the sensitivity or frequency stability of the AFM itself. We thus conclude that time resolution in our experiments is limited by the pulse length of the pump and probe and not by the AFM detector.

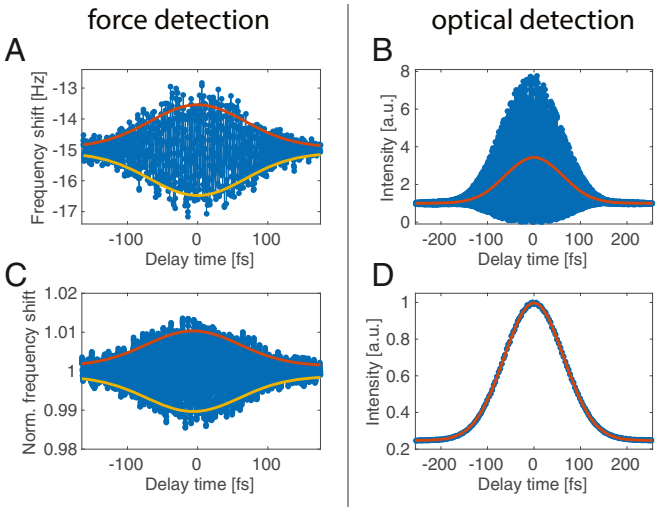

Fig. 2. Frequency shift of the FM-AFM measurement with (*A*) collinear and (*C*) noncollinear laser configuration; the signal is generated by the polarization change in $LiNbO_3$ while the two laser beams are delayed with respect to each other. A pulse width of 108.6 ± 3.8 fs is recovered, illustrated by the fit of the lower (yellow) and upper (red) envelope. Concurrently retrieved (*B*) optical interferometric and (*D*) intensity autocorrelation traces, recorded using a photodiode placed before the UHV chamber. Using a Gaussian profile, a pulse width of 106.5 ± 0.2 fs is measured in both cases. The red solid line is showing the fit to the intensity autocorrelation, in *B*, extracted by low-pass filtering.

Power-, Polarization-, and Distance-Dependent tr-AFM Measurements. To further characterize the tr-AFM signal and its light-induced origin, various optical power-, polarization-, and tip–sample distance-dependent measurements are performed. First, the amplitude of the signal is recorded at different tip–sample distances to determine how the tr-AFM signal decays along the surface normal. The same measurements were performed using

PHYSICS

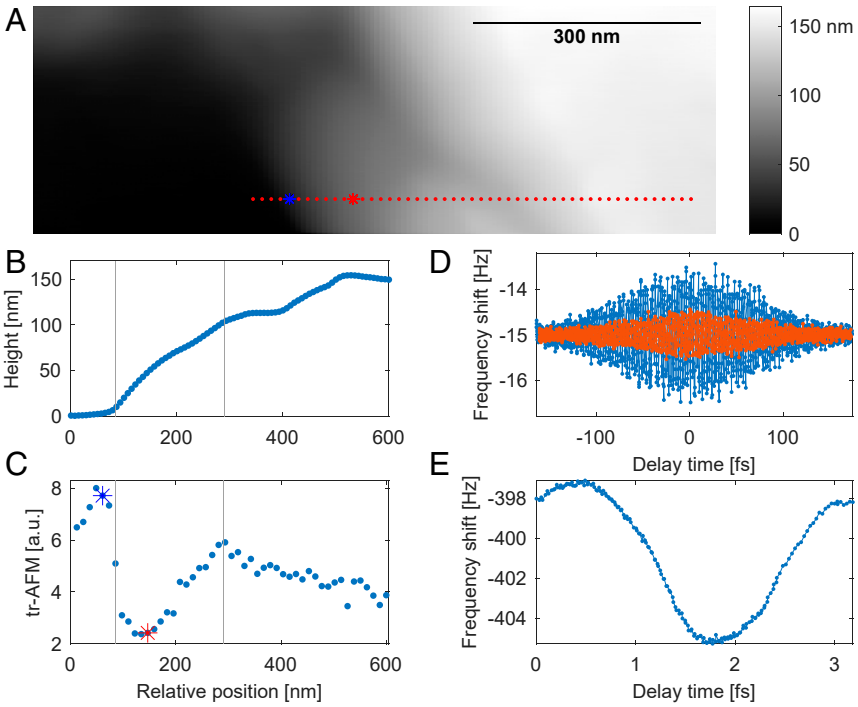

Fig. 3. Spatially resolved measurement of the ultrafast light-induced AFM signal. (*A*) The topography is shown, indicating the position of the line scan. At each point (separated by 12.25 nm), a full delay scan is performed. (*C*) The oscillation amplitude is plotted at each point, with (*B*) the extracted topography. The vertical lines indicate the extent of the surface adsorbent. (*D*) Raw data from the tr-AFM scans are shown, corresponding to the red and blue markers in the line scan (*A* and *C*), respectively. (*E*) Constant height nc-AFM measurement with minimal achievable delay. The full oscillation can be clearly resolved with a minimum resolvable step size of about ~ 25 as.

s and p polarization. When p polarization is used (Fig. 4*B*), the tip–sample force extends over a range of 700 nm, while, with s polarization, it decays toward 0 frequency shift within 200 nm. This can be explained by the surface or bulk response when using s or p polarization, respectively. Lithium niobate exhibits a surface nonlinear response resulting in a p polarization when driven with s polarization (9). This surface response is observed to be weaker in amplitude, as seen with s polarization in our measurement (Fig. 4). In Fig. 4*A*, the normal FM-AFM frequency shift signal follows the same trend. Both the tr-AFM and the regular nc-AFM distance-dependent spectra are fit to the electrostatic force from Eq. **4** with a tip–sample capacitance according to ref. 10 (see *Materials and Methods* for details). The distance-dependent results in Fig. 4*A* show that the photoinduced signal is present at both small and large gap spacings, and thus cannot be due to a thermal expansion effect of the tip or sample. Additional evidence of the electrostatic nature of the signal is given by a measurement on an island of $MoSe_2$ shown in *SI Appendix*, Fig. S1*C*. The symmetry breaking of odd-layer $MoSe_2$ is expected to yield a $\chi^{(2)}$ response and an enhanced SHG for

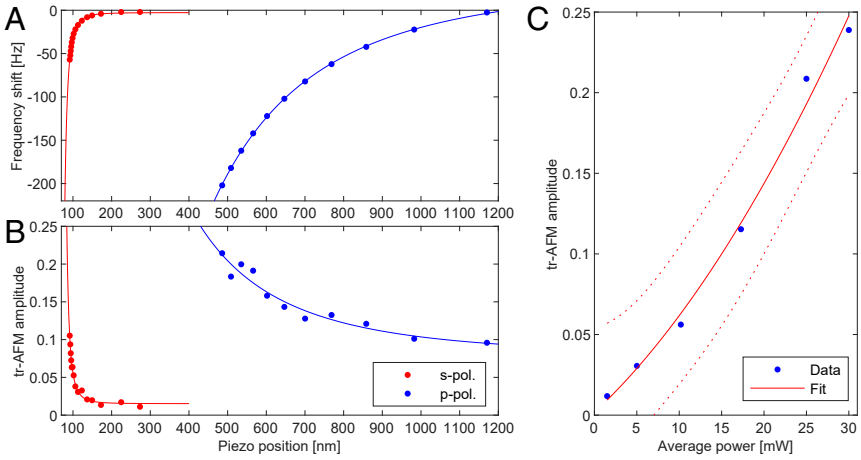

Fig. 4. (*A* and *B*) Frequency shift and tr-AFM signal amplitude vs. z-piezo position for two different optical polarizations. S polarization corresponds to the most optimal excitation along the z direction of the PPLN crystal, resulting in a stronger light-induced polarization. All measurements are fitted (solid line) to an electrostatic model. (*C*) Power-dependent measurement of the tr-AFM signal. A second-order polynomial is fitted to the data according to Eqs. **2** and **3**.

two-photon absorption on resonant pumping (11). On the $MoSe_2$ island, we observe a strong signal oscillating at the pump carrier wave period of 2.6 fs with an envelope determined by the pump pulse duration at the pulse overlap, while a reference measurement on the SiO_2 substrate does not show any resolvable signal. The lack of a signal on the silicon substrate indicates that the signal cannot originate from a light-induced tip–sample distance modulation, or an expansion of the tip, as these effects would not vanish when moving from $MoSe_2$ to the silicon substrate.

The tr-AFM signal was also measured as a function of the input laser power, as shown in Fig. 4*C*. The observed behavior can be fit by Eqs. **2** and **3**. Note that the second-order polarization depends linearly on the intensity of the input beams. This second-order polarization leads to an additional term in the tip–sample potential (Eq. **3**), whereby $\Delta f \propto (V_{cpd} - V_{dc} - \phi_{pol}/e)^2$ and $\phi_{pol} \propto P^{(2)}_{OR}(t,\tau) \propto (E)^2$. From the data presented in Fig. 4, we conclude that the measured ultrafast tr-AFM interaction is electrostatic in nature. The origin of this electrostatic field is sample-specific nonlinear polarization responses to illumination.

Discussion

In summary, we show that force measurements can be used to detect the 100-fs laser pulse-induced polarization response in a material. Surprisingly, the time resolution of this force measurement is limited by the laser pulse length, and not by the 300-kHz AFM cantilever resonance frequency. Scanning the AFM tip then allows mapping of the spatial variation of the sample response. In particular, we have observed a large change of the polarization response of a PPLN crystal over a distance of 15 nm. By imaging the response of a few layers of $MoSe_2$ and the SiO_2 substrate, we demonstrate that tr-AFM measures the local sample response, and can exclude thermal or optically induced artifacts such as tip–sample separation variations. By controlling the light polarization, we are able to distinguish between different nonlinear effects and their contribution to the overall measured force.

From our experiments, we conclude that the χ^2 response of nonlinear materials can be spatially resolved with AFM. However, this is not limited to a χ^2 response. Any optically induced change which results in a nonzero averaged electric field at essentially zero frequency, such as shift or injection currents in semiconductors and four-wave mixing processes, should be measurable via a force measurement with nanometer spatial resolution and temporal resolution limited by the pump–probe characteristics. Using well-established pump–probe methods, we predict that localized force detection by tr-AFM will become a powerful method for studying the spatial distribution and correlations of inhomogeneities and defects on a nanometer length scale and their effect on ultrafast charge dynamics. This will, in particular, allow the detailed study of the role of defects in optoelectronic materials, such as transition metal dichalcogenides, organic thin films, or wide-bandgap semiconductors for PHz electronics. Experiments of ultrafast electron dynamics with nanometer real-space resolution will allow the validation of ab initio modeling without the need for interpolation over many orders of magnitude in space-time.

Force probing of the nonlinear optical response at the nanometer scale is insensitive to phase matching conditions, making nonlinear optical experiments less challenging. The presented tr-AFM detection of nonlinear optical responses complements emerging scanning probe techniques, such as THz scanning tunneling microscopy (12–15), photoinduced force microscopy (16–18), scanning near-field optical microscopy (14, 19–21), or AFM for surface voltage measurements (22–24), to investigate light–matter interactions on the nanoscale with high temporal resolution.

Material and Methods

AFM Setup. A commercial JEOL JSPM-4500A UHV system with a cantilever beam deflection AFM configuration is used in this study. A band-pass filter is mounted in front of the four-quadrant photodiode of the deflection system to prevent stray light from the femtosecond laser interfering with the AFM measurement. A Nanonis OC4 system is used for control of the AFM. The femtosecond-pulsed laser is coupled into the UHV chamber via a home-built in-vacuum beam steering system, consisting of a mirror on a sphere controlled by stick–slip piezo motors. The laser spot size on the sample surface is approximately 900 μm by 200 μm, with an estimated 2,000 to 9,000 photons per probe area (assumed to be a 10-nm-diameter circle) in 10 ms, depending on the average power used.

Fast Fourier Transform Analysis for tr-AFM Amplitude Extraction. A fast Fourier transform (FFT) is performed on the frequency shift versus delay time data. From the FFT, the peak amplitude around 384 THz is extracted, which corresponds to the wavelength of the incident laser. The delay scan is performed with the highest resolution of the linear delay stage of 0.6 fs. The raw data are downsampled from 0.6-fs step size to 1.2-fs step size to prevent any false frequency response due to randomly missed/double steps of the delay stage.

Single-Cycle Measurement. The single-cycle measurement was performed while the z feedback was turned off. The tip was lifted by 0.5 nm from –400-Hz frequency shift set point and held at a constant piezo position while the delay was swept. It was verified that, during the full sweep of the delay, no significant drift of the piezo occurs. The temporal delay between the pulses is controlled by a linear delay stage (Thorlabs ODL220). To achieve delays below 0.6 fs, two quartz wedges are used: One wedge is fixed while the second is moved into the beam path to generate an overall delay in the beam with a minimal step size of a few tens of attoseconds.

Distance-Dependent Measurement. The distance-dependent measurements were performed by approaching to different frequency shift set points ranging from –222 Hz to –2 Hz. The delay scan is performed with the z feedback on with a very slow feedback loop to just correct for long-term drift as a delay scan over the full pulsed overlap is recorded. The average z position is used for determining the tip–sample distance, with the closest approach set to 0 nm. One should note that this does not reflect the absolute tip–sample distance. The polarization was rotated by 90° (s polarization) using a polarizer and wave plate to keep the power constant at 22.3 mW and 22.8 mW, respectively.

For fitting the electrostatic model, we use (10) $F_z(z) = \pi\epsilon_0[R^2/(z(z+R))]V^2$. In first approximation, we use the first derivative of the force to describe the frequency shift, resulting in a fitting function

$$\Delta f \propto \pi\epsilon_0 \left[\frac{R^2(R+2z)}{z^2(z+R)^2}\right] V^2. \quad [4]$$

Contribution of Second-Order Polarization to the Measured Frequency Shift. As mentioned in the *Results*, Eq. **1**, for the second-order nonlinear polarization, results in the expression for multiple nonlinear processes. They can be written as

$$P^{(2)}(t) =$$

$$2\epsilon_0\chi^{(2)}[E(t)E(t)^* + E(t+\tau)E(t+\tau)^*] \quad (OR \text{ or } P^{(2)}_{OR}(t)) \quad [5]$$

$$+ \epsilon_0\chi^{(2)}\left[E(t)^2 e^{-2i\omega t} + E(t+\tau)^2 e^{-2i\omega(t+\tau)} \quad (SHG) \right. \quad [6]$$

$$+ 2E(t)E(t+\omega)e^{-i(\omega t+\omega(t+\tau))} \quad (SFG) \quad [7]$$

$$\left. +2E(t)E(t+\tau)^* e^{-i(\omega t-\omega(t+\tau))} + c.c.\right] \quad (DFG \text{ or } P^{(2)}_{OR}(t,\tau)). \quad [8]$$

The respective processes for each term are labeled to the right. The *OR* term from each beam will lead to a background which can be seen by the DC

PHYSICS

filter signal in *SI Appendix*, Figs. S2 and S4. The *SHG* and *SFG* terms both oscillate in time, but do not lead to a DC offset measured by our setup. Due to the zero frequency difference between the two laser pulses, the *DFG* term is not oscillating in real time. However, it is oscillating in delay time as shown in Eq. **2**. The *OR* ($P^{(2)}_{OR}(t)$) and *DFG* ($P^{(2)}_{OR}(t,\tau)$) terms are therefore the two processes we measure in our setup.

$$F_{elec} = \frac{1}{2}\frac{dC}{dz}\left(V_{cpd} - V_{dc} - \left(\frac{\phi_{OR}(t)}{e} + \frac{\phi_{OR}(t,\tau)}{e}\right)\right)^2. \quad [9]$$

The polarization term $\phi_{OR}(t,\tau)$ leads to an oscillation in delay time (Eq. **8**), while the $\phi_{OR}(t)$ term leads to a DC offset with no modulation in delay time (Eq. **5**). This allows us to distinguish these two different terms in the AFM measurement and treat $\phi_{OR}(t)$ as a simple electrostatic background together with V_{cpd} as V_{BG}.

Due to the quadratic contribution to the force, $\phi_{OR}(t,\tau)$ will also contribute with a quadratic component $\phi_{OR}(t,\tau)^2$ and a $\phi_{OR}(t,\tau)*V_{BG}$ component. The $\phi_{OR}(t,\tau)^2$ term will exhibit a nonsymmetric shape in frequency shift and have a component at zero frequency with a modulation following the pulse envelope (*SI Appendix*, Fig. S4). The relative strength between the $\phi_{OR}(t,\tau)$ and V_{BG} components can alter the final signal toward a symmetric or nonsymmetric shape, depending on the strength of the electrostatic background, including the one-beam $\phi_{OR}(t)$ term. A strong V_{BG}, as observed in the lithium niobate sample by the large frequency shift and long approach curves, will lead to a stronger $\phi_{OR}(t,\tau)*V_{BG}$ over the $\phi_{OR}(t,\tau)^2$ contribution, resulting in the observed symmetric signal in lithium niobate. Comparable strength between the background and two-beam polarization $\phi_{OR}(t,\tau)$ term leads to an asymmetric signal in frequency shift with a DC component following the pulse envelope, like observed in $MoSe_2$.

Based on Eqs. **1** and **3**, we can qualitatively model the response expected from $P^{(2)}_{OR}(t)$ and $P^{(2)}_{OR}(t,\tau)$. Note that the polarization term $P^{(2)}_{OR}(t,\tau)$ leads to an oscillation in delay time with the period corresponding to the light frequency (Eq. **7**), while the $P^{(2)}_{OR}(t)$ term leads to a DC offset with no modulation in delay time (Eq. **4**). The two contributions are thus present at different frequencies in delay time, and a Fourier analysis can be used to distinguish and quantify their respective contributions. *SI Appendix*, Fig. S2 shows the Fourier-filtered signal for the lithium niobate (SI Appendix, Fig. S2*E*), and the $MoSe_2$ sample (*SI Appendix*, Fig. S2*G*). The measured results can qualitatively be reproduced by our model including a strong electrostatic background. As mentioned above, a strong electrostatic background (*SI Appendix*, Fig. S2*B*) leads to a symmetrical response in frequency shift; the DC Fourier component at pulse overlap is strongly damped (*SI Appendix*, Fig. S2*F*). Assuming a weak electrostatic background (*SI Appendix*, Fig. S2*D*) results in an asymmetric shape in frequency shift and a noticeable signal in the DC component at pulse overlap. This qualitatively matches the measurement on $MoSe_2$ (*SI Appendix*, Fig. S2*C*). The strong electrostatic background in the lithium niobate manifests itself by the long approach curves and high-frequency shift set point needed to reach imaging condition close to the surface.

Spatially Resolved Measurement. The AFM tip is held at constant frequency shift with a slow z feedback to correct for long-term drift during the delay scan at each point. From each delay scan, the tr-AFM signal amplitude is extracted according to the FFT analysis explained above. The extracted tr-AFM amplitude is normalized by the optical autocorrelation intensity to account for any small fluctuation in laser power (average 7.29 mW) during the measurement time.

AFM Autocorrelation. In our experiment, a metal-coated silicon tip (Nanosensors, PPP-NCHPt, f_0 = 297.6 kHz, Q = 12,524) is approached to the sample surface. A measured normalized frequency shift ($\Delta f/\text{mean}(\Delta f)$) is shown in Fig. 2*C*. The tr-AFM signal can be recorded in multiple modes, like any other spectroscopy technique in AFM. The measurement shown in Fig. 2*A* is recorded with a very slow z feedback to correct for slow drift, but the feedback is not fast enough to compensate for the frequency shift change due to the pulse overlap. For the measurement in Fig. 2*C*, the AFM tip is held at a constant height above the sample, while the beam delay is swept. The tip is occasionally approached to the surface to correct for any drift in the tip–sample distance. Fig. 2*D* shows an optical intensity autocorrelation trace recorded simultaneously outside of the UHV chamber (Fig. 1*A*). The envelopes of both curves are fit to a Gaussian profile, and this yields a pulse width of 106.5 ± 0.2 fs for the optical intensity autocorrelation. The envelope measured by FM-AFM shows a pulse width of 108.6 ± 3.8 fs. The observed pulse broadening can be accounted for by the dispersion that arises from the UHV window and the lens used to focus the beam into the UHV chamber. $LiNbO_3$ as a sample can therefore be used to characterize the pulse shape at the tip apex.

Optical Autocorrelation. A β-barium borate crystal is used for optical autocorrelation measurements through *SHG* for both intensity (noncollinear) and interferometric (collinear) autocorrelation as shown in Fig. 1. A photodiode is used for detection of the second harmonic signal, with either a spatial or low-pass filter to separate the signal from the fundamental. A Gaussian pulse is fitted to extract the pulse duration. An FFT with a low-pass filter is applied to the interferometric autocorrelation to extract the intensity autocorrelation contribution. Built-in envelope extraction is used in MATLAB to extract the envelope of the AFM autocorrelation signal. The same fitting procedure used for the optical autocorrelation is applied to the extracted envelope to retrieve the pulse width.

Chopper Measurements. The measurements on $MoSe_2$ are performed with a chopper wheel in one arm of the interferometer. The use of the chopper wheel results in the modulation of the AFM frequency shift at the chopper frequency. This modulation is detected with a Zurich Instruments lock-in amplifier (UHF). The lock-in signal is directly proportional to the effects due to illumination without any artifacts due to drift of the AFM tip during tip lift measurements (25).

Lithium Niobate. The z cut of the crystal, in conjunction with p-polarized incident light, allows for the strongest induced polarization occurring along the surface normal.

$MoSe_2$ Sample Fabrication. The monolayer $MoSe_2$ was obtained by using an all-dry polydimethylsiloxane (PDMS) transfer technique. For this, bulk $MoSe_2$ (HQ Graphene) was first mechanically exfoliated onto a PDMS substrate and subsequently transferred on a silicon substrate with a 285-nm SiO_2 capping layer. The thickness of the flake was determined by optical contrast.

Data Availability. All relevant data supporting the findings of this study are available at Figshare (https://doi.org/10.6084/m9.figshare.12478334).

ACKNOWLEDGMENTS. We acknowledge Christopher Phillips for providing the PPLN sample. This work was supported by Natural Sciences and Engineering Research Council of Canada, Fonds de recherche du Québec – Nature et technologies, and Canada Foundation for Innovation.

1. M. Peplow, The next big hit in molecule Hollywood. *Nature* **544**, 408–410 (2017).
2. A. Dhar, A. Mansingh, Optical properties of reduced lithium niobate single crystals. *J. Appl. Phys.* **68**, 5804–5809 (1990).
3. M. Bass, P. A. Franken, J. F. Ward, G. Weinreich, Optical rectification. *Phys. Rev. Lett.* **9**, 446–448 (1962).
4. R. W. Boyd, *Nonlinear Optics* (Academic, ed. 3, 2008).
5. A. Liscio *et al.*, Quantitative measurement of the local surface potential of π-conjugated nanostructures: A Kelvin probe force microscopy study. *Adv. Funct. Mater.* **16**, 1407–1416 (2006).
6. S. A. Burke *et al.*, Determination of the local contact potential difference of PTCDA on NaCl: A comparison of techniques. *Nanotechnology* **20**, 264012 (2009).
7. T. R. Albrecht, P. Grütter, D. Horne, D. Rugar, Frequency modulation detection using high-Q cantilevers for enhanced force microscope sensitivity. *J. Appl. Phys.* **69**, 668 (1991).
8. N. Argiolas *et al.*, A systematic study of the chemical etching process on periodically poled lithium niobate structures. *Mater. Sci. Eng. B* **118**, 150–154 (2005).
9. T. J. Sono *et al.*, Reflection second harmonic generation on a z-cut congruent lithium niobate crystal. *Phys. Rev. B* **74**, 205424 (2006).
10. S. Hudlet, M. Saint Jean, C. Guthmann, J. Berger, Evaluation of the capacitive force between an atomic force microscopy tip and a metallic surface. *Eur. Phys. J. B* **2**, 5–10 (1998).
11. C. Tam Le *et al.*, Nonlinear optical characteristics of monolayer MoSe 2. *Ann. Phys.* **528**, 551–559 (2016).
12. T. L. Cocker *et al.*, An ultrafast terahertz scanning tunnelling microscope. *Nat. Photon.* **7**, 620–625 (2013).
13. T. L. Cocker, D. Peller, P. Yu, J. Repp, R. Huber, Tracking the ultrafast motion of a single molecule by femtosecond orbital imaging. *Nature* **539**, 263–267 (2016).
14. M. A. Huber *et al.*, Femtosecond photo-switching of interface polaritons in black phosphorus heterostructures. *Nat. Nanotechnol.* **12**, 207–211 (2016).
15. V. Jelic *et al.*, Ultrafast terahertz control of extreme tunnel currents through single atoms on a silicon surface. *Nat. Phys.* **13**, 591–598 (2017).
16. J. Jahng *et al.*, Gradient and scattering forces in photoinduced force microscopy. *Phys. Rev. B* **90**, 155417 (2014).

17. J. Jahng *et al.*, Ultrafast pump-probe force microscopy with nanoscale resolution. *Appl. Phys. Lett.* **106**, 083113 (2015).
18. B. T. O'Callahan, J. Yan, F. Menges, E. A. Muller, M. B. Raschke, Photoinduced tip–sample forces for chemical nanoimaging and spectroscopy. *Nano Lett.* **18**, 5499–5505 (2018).
19. V. Kravtsov, R. Ulbricht, J. M. Atkin, M. B. Raschke. Plasmonic nanofocused four-wave mixing for femtosecond near-field imaging. *Nat. Nanotechnol.* **11**, 459–464 (2016).
20. M. Eisele *et al.*, Ultrafast multi-terahertz nano-spectroscopy with sub-cycle temporal resolution. *Nat. Photon.* **8**, 841–845 (2014).
21. T. Jiang, V. Kravtsov, M. Tokman, A. Belyanin, M. B. Raschke, Ultrafast coherent nonlinear nanooptics and nanoimaging of graphene. *Nat. Nanotechnol.* **14**, 838–843 (2019).
22. D. C. Coffey, D. S. Ginger, Time-resolved electrostatic force microscopy of polymer solar cells. *Nat. Mater.* **5**, 735–740 (2006).
23. M. Takihara, T. Takahashi, T. Ujihara, Minority carrier lifetime in polycrystalline silicon solar cells studied by photoassisted Kelvin probe force microscopy. *Appl. Phys. Lett.* **93**, 021902 (2008).
24. Z. Schumacher, Y. Miyahara, A. Spielhofer, P. Grutter, Measurement of surface photovoltage by atomic force microscopy under pulsed illumination. *Phys. Rev. Appl.* **5**, 044018 (2016).
25. Z. Schumacher, A. Spielhofer, Y. Miyahara, P. Grutter, The limit of time resolution in frequency modulation atomic force microscopy by a pump-probe approach. *Appl. Phys. Lett.* **110**, 053111 (2017).